Precise control over gas transporting channels in zeolitic imidazolate framework glasses

Oksana Smirnova[1,#], Seungtaik Hwang[2,#], Roman Sajzew[1], Aaron Reupert[1], Vahid Nozari[1], Samira Savani[1], Christian Chmelik[2], Lothar Wondraczek[1,3], Jörg Kärger[2], Alexander Knebel[1,3,*]

# These authors contributed equally

* Corresponding author
alexander.knebel@uni-jena.de

[1]University of Jena, Otto Schott Institute of Materials Research, Fraunhoferstasse 6, 07743 Jena, Germany.

[2]University of Leipzig, Faculty of Physics and Earth Sciences, Linnéstraße 5, 04103 Leipzig, Germany.

[3]Center of Energy and Environmental Chemistry – CEEC Jena, University of Jena, Philosophenweg 7a, 07743 Jena, Germany.

Abstract

Porous materials, such as metal-organic frameworks emerge to solve important quests of our modern society, such as CO_2 sequestration. Zeolitic Imidazolate Frameworks (ZIFs) can undergo a glass transition to form ZIF-glasses; they combine the liquid handling of classical glasses with tremendous potential for gas separations. Using millimeter-sized ZIF-62 single crystals and centimeter-sized ZIF-62-glass we demonstrate scalability and processability. Further, following the evolution of gas penetration into ZIF-crystals and ZIF-glasses by IR microimaging techniques enables to determine diffusion constants and changes to the pore architecture on the Ångström-scale. The evolution of ZIF-glasses is observed *in situ* using a microscope heating stage. The pore-collapse during glass-processing is tracked by changes to density and volume of the glasses. Mass spectrometry investigates the crystal-to-glass transition and thermal processing ability.

Introduction

As the industrial interest in porous metal-organic frameworks (MOFs) rises, highly developed MOF materials, as well as MOF-derived materials have been found. The combination of the complex properties of the inorganic-organic hybrid MOFs with another class of materials shifts paradigms of both materials' worlds. Some examples are carbonized MOF lattices for catalytic applications from controlled burning of MOFs (*1*) or liquids with permanent porosity to achieve liquid processability and accessible porosity inside a solvent (*2, 3*). One of the most promising new materials originates from the MOF-subclass of zeolitic imidazolate frameworks (ZIFs), which was found to be meltable. This nucleated the field of hybrid MOF-glasses less than ten years ago (*4, 5*). The earliest examples of glass usage by humankind date back more than 30.000 years; since then, glasses have triggered a range of societal revolutions. Hybrid materials obtained from MOFs or other types of coordination compounds have been identified as the next potential breakthrough, enabling new horizons in energy and environmental technology, catalysis and water harvesting (*6*). As the fundamental idea, it was proposed that ZIF-glasses combine the porous features of MOFs and the universal processability of classical glasses in their liquid state (*2*). However, the residual pore architecture in ZIF-glass is not understood yet, and glass-like melt processing of MOF objects or products has not been demonstrated to date. While a range of properties typical for glassy materials (such as mechanic performance) have been tested on solid MOF-glass specimens (*7, 8*), the fundamental question of porosity in these glasses remained unresolved.

Here, we show that ZIF-glasses indeed lay the foundation for completely novel applications of glasses in gas separation, as they offer tailorable molecular sieving properties to a higher precision than it can be achieved using conventional reticular MOF chemistry (*9*). The possible disruptive impact of a molecular sieving material with highly defined size exclusion is immense (*10*), as it allows to tackle all kinds of separation tasks, from methane valorization and carbon capture (*11*) to other technologies operating at the limits of size exclusion sieving , such as propylene/propane separation (*12*).

Crystalline ZIFs are already outstanding molecular sieves and are very well suited for gas separation in membranes, even though they face a few common MOF problems because of their soft-porous nature (*2, 12*). The glass transition of ZIFs was a novel discovery, originally made on ZIF-4. It was proposed and later confirmed through X-ray scattering experiments that the associated melt-quenched ZIF glasses exhibit free-space cavities (*13*). Since then, other ZIFs and TIFs (tetrahedral imidazolate frameworks), such as TIF-4, ZIF-62, ZIF-76 and ZIF-8 have been found to be meltable. A logical approach toward porous glasses has been taken with ZIF-8 and ZIF-76, which show sodalite cages with high porosity (*14, 15*). To make both materials meltable, assistance by a flux-mediator is necessary because thermal decomposition would otherwise occur before their large pores destabilize. For example, ZIF-76 needs a melt of ZIF-62 or TIF-4 as a mediator, making it difficult to determine the exact material porosity after melt-quenching (*15*). Surface-mediated melting through imidazole-based ionic liquids is another option, which helps to transform ZIF-8 into a glass, and also helps to melt ZIF-76 (*16*).

Nevertheless, residual ionic liquid left within the compound leads to a high amount of non-accessible porosity, and may also end up as partially decomposed guest inside the glass (*17*). For ZIF-62 - probably the best-known MOF-glass former to date, currently available data does not allow for clear conclusions as to the nature and architecture of residual pores in its glassy state. ^{67}Zn-NMR seems to prove that there is no short-range order in ZIF-62 glass and, thus, no leftover porosity in re-melted glasses to resemble its MOF origin (*18*). On the other hand, conflicting conclusions were drawn from X-ray scattering experiments for glasses derived directly from the crystalline state (*19*). Permanent gas and hydrocarbon uptake into the framework of ZIF-62 and pores as big as 9 Å were reported for ZIF-62-glasses. ZIF-62 has been synthesized on ceramic supports, and the glasses made of it achieve pore-cutoffs at about 3.3 Å (*20*); similarly ZIF-4/TIF-4 allows to separate gases in a membrane film (*21*).

The route to ZIF-62, and from a crystal to a_gZIF-62 (a_g = amorphous glass) differs from scientist to scientist. Often described are problems in phase-purity, where ZIF-zni phases occur during synthesis (*22*). Even smallest impurities are known to potentially result in strong variations of material properties, for example, in thermal stability or optical appearance (*7, 23*). We find that decomposition products can act as blowing agents, which could lead to larger pores. Notable variations in thermal processing methods, such as melt-quenching rates, re-melting of the glass or direct collapse of the MOF could be the reason why some groups report non-porous glasses, while others predict MOF-like features (*24*). Porosity being key to any of the anticipated applications of MOF glasses, thermal processing of high-quality glasses is a prerequisite for breaking-through on this issue. However, currently reported MOF-glasses suffer from significant material quality issues, including – aside contamination and phase impurity - bubble formation, (micro-)cracking, surface oxidation and partial decomposition (*25*). Multiple remelting – a standard in high-quality optical glass manufacture – is not possible for MOF glasses when MOF properties are to be retained to the largest possible extent.

To us, the biggest misconception in terms of porosity determinations in the ZIF-glasses is the frequently applied volumetric gas adsorption to determine surface areas and pore volumes. MOFs (such as ZIF-62) with already low surface areas and pore volumes, showing even 50% less porosity in the glass (*26*) are certainly not interesting for adsorptive gas separation, e.g., in comparison to MOFs such as CALF-20 (Calgary Framework 20) (*27*). But for membrane separation, the plain molecular sieving properties are of highest interest; pore volume and surface areas are only secondary parameters. Our goal was to develop a methodology to distinguish between the mature, low-entropy ZIF-62 glass - a non-porous, collapsed system - and the juvenile, high-entropy ZIF-62-glass with open pore channels. What we are looking at is not the amount of gas that can be taken up by these glasses, but the number of pathways a gas can take and how these are altered upon liquid processing. The kinetic gas uptake and molecular diffusion are what makes these glasses interesting; we developed a scalable synthesis route for phase-pure ZIF-62 and base our kinetic gas diffusion measurements solely on millimeter-sized single crystals of ZIF-62 and cm-scale glasses, measuring gas diffusion *in situ* through infrared microscopy (IRM). We find strong dependencies of the diffusivities on the parameters applied during glass processing,

respectively, the underlying changes of pore channels. This technique has been applied successfully for zeolites and, later, crystalline ZIF materials, and is particularly feasible for mixed-linker systems(*28*) such as ZIF-62. It is also feasible to fully characterize glasses (*29*) and the gas transport properties in nanoporous materials following Fick's laws of diffusion (*30*). We now understand the evolution of the gas transporting pore-channels upon processing of ZIF-glasses, and we were even able to find strong evidence that by our methods, the gas transport properties can be altered in a controlled way until a total size exclusion for a large gas species is achieved. The reported synthetic procedures and the liquid-processing of ZIF-62 in its glassy state allow for scalable, processed MOF-glass. This paves the way for large-area, free-standing molecular sieving ZIF-glass films. These could help to solve a range of urgent problems, such as carbon capture or efficient hydrocarbon separations, and could potentially enable future fields of interest in gas separation, for instance, direct capture of CO_2 or He from air (*31*).

Results

Development of a scalable synthesis procedure for porous ZIF-62 and ZIF-62 glasses

Previously reported mixed-linker ZIF-62(Zn) synthesis (structure is shown in **Fig. 1A**) commonly was performed in small batches (*25, 26*) and, as well as commercially sold ZIF-62, had the problem of severe phase-impurities, mainly the ZIF-zni phase (*22*). Some important improvements were applied to develop a scalable synthesis for high yield, phase pure ZIF-62.

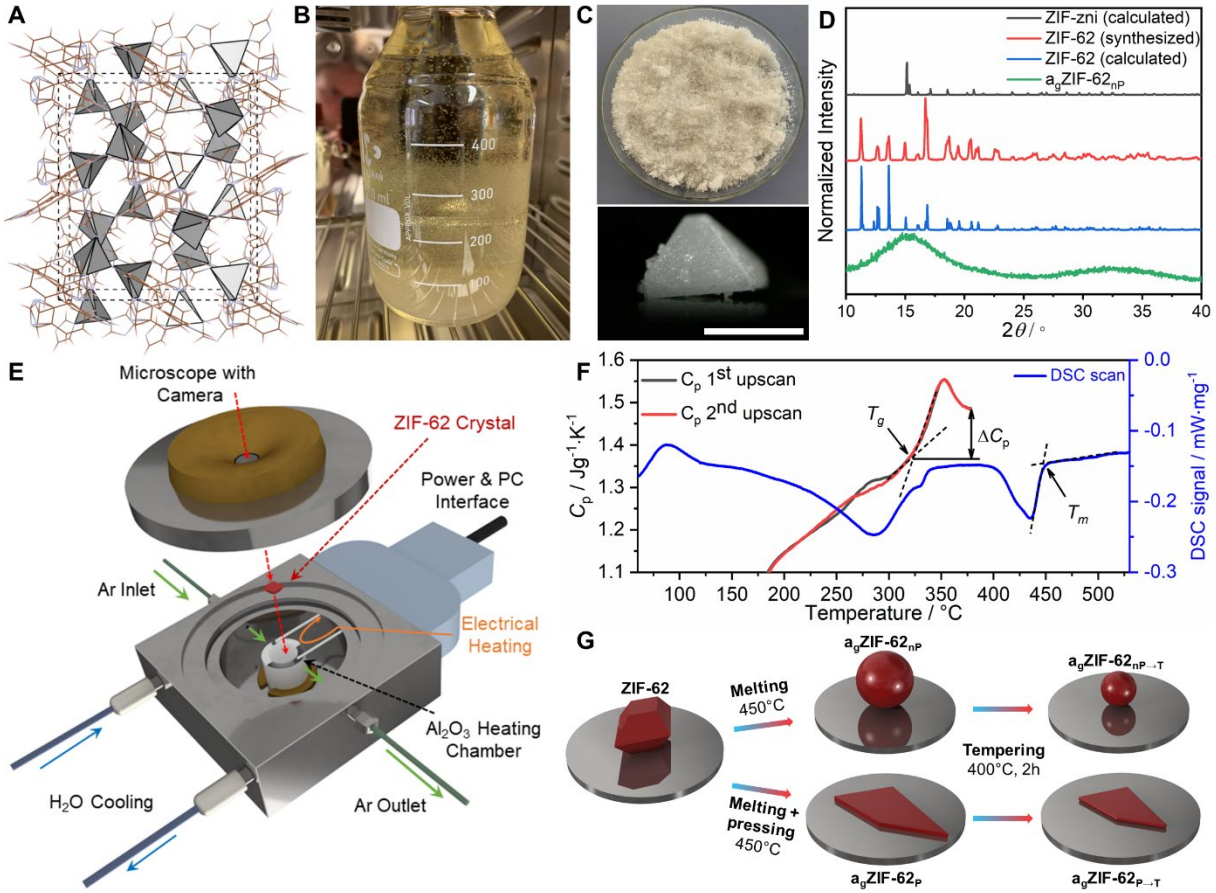

Fig. 1 (A) Crystal structure of ZIF-62 in a-direction. **(B)** Photograph of the upscaled ZIF-62 synthesis with large crystals growing on the walls. **(C)** Photograph of as synthesized 10 g ZIF-62(Zn) from a single batch synthesis and micrograph of a typical crystal; scalebar is 1 mm. **(D)** PXRD data of ZIF-62 and a_gZIF-62$_{nP}$ and simulated ZIF-zni and ZIF-62. **(E)** Schematic of the *in situ* heating stage for the optical microscope. **(F)** DSC signal to determine T_m of the ZIF-62 batch and cyclic scans of the heat capacity c_p with heating and cooling rates of 20 K/min to determine T_g. **(G)** Flowchart for the melt-processing applied to ZIF-62 in this study. ZIF-62 and derived materials are shown in red.

Our upscaled synthetic procedure (**Fig. 1**, **B** and **C**, **SI**) results in 10 g (15 g in total after reusing the mother liquor twice) of phase-pure ZIF-62(Zn) from 480 ml of DMF with crystals up to 2 mm in size (**Fig. 1C**, **S1** and **S2**). First, the mixing technique was changed: instead of preparing the stock solutions as it has been frequently reported (*19, 24, 25, 32*), a direct preparation was used. We chose the highest purity grade chemicals (especially imidazole) and added the two ligands one by one, followed by adding Zn^{2+} to the well homogenized mixture

(**SI**). Inhomogeneous mixing with imidazole(Im)-rich regions would lead to zni-phase crystallization (*22*). Structure and phase purity of the as-synthesized ZIF-62 (ratio of benzimidazole (bIm) to imidazole (Im) = 1:4.8) calculated from NMR (**Fig. S3**) and formation of a_gZIF-62 was confirmed using PXRD and simulated patterns (**Fig. 1D**). The synthetical scale-up is also possible for ZIF-62(Co) (**Fig. S4** to **S9**), but the material is not further investigated in this report**.** In particular, the washing and drying procedures are of key importance for obtaining high-quality ZIF-62 materials. ZIF-62(Zn) was properly cleaned with dichloromethane, and dried using a vacuum oven, allowing for accessible porosity with only 0.02 DMF molecules per unit cell remaining as determined by ^{1}H-NMR (**Fig. S5**). This amount of DMF seems to be crucial for the crystal structure, as shown later. DSC (differential scanning calorimetry) and c_p (heat capacity) (**Fig. 1F**) show the melting point (T_m) and the glass transition temperature (T_g). As ZIF-62 has a high purity, a 10-30K increase to previously reported melting temperature (now T_m = 450°C) (*19, 22, 33*) and glass transition temperature T_g (now 322°C) (*4, 5, 15, 22, 26, 34*) is found.

Melting *in situ* with a microscope-coupled heating stage was performed in an Ar atmosphere using single crystals (**Fig. 1E**); the flow chart in **Fig. 1G** describes our procedures. Properly washed and vacuum-dried ZIF-62 then formed transparent and nanoporous glasses upon melting (**SI Methods**). Room temperature drying or just heating under ambient conditions was not enough for sufficient activation, because the narrow pores of ZIF-62 released residual DMF molecules only very slowly. We think that problems, such as bubble formation (*19, 25, 32*) and even exploding crystals (**Movie S1**) may occur because of decomposition of excess residual DMF that acts as blowing agent. Here, we obtained transparent a_gZIF-62$_{nP}$ (nP = not pressed) (**Movie S2** and **Movie S3**), while applying pressure to the sample during the melting process yielded flat homogeneously transparent glass pieces, denoted a_gZIF-62$_P$ (P = pressed) (**Fig. S10** and **S11**). Both a_gZIF-62$_{nP}$ and a_gZIF-62$_P$ were further processed by tempering at 400 °C *in situ* (further a_gZIF-62$_{nP\rightarrow T}$ (**Movie S4**) and a_gZIF-62$_{P\rightarrow T}$ (**Movie S5**) respectively) (**Fig. 1G**). *Ex situ* optical micrographs were always taken before and after the processes (**Fig. S12** to **S16**).

Kinetic gas uptake in processed a_gZIF-62

Kinetic gas uptake was measured for 0-40 mbar CO_2 and 0-200 mbar ethane, and their diffusion into the sample matrix was followed by IR microscopy (IRM) (**Fig. 2**, **A** and **B**, **S17** to **S21**) (*29, 30*). Each measurement was performed with only one unit of the sample (e.g. single crystal, glass shard) to avoid grain boundary diffusion. We show a pore diffusion schematic next to each sample, which was developed following the results obtained in this study (**Fig. 2**, **C** to **E**).

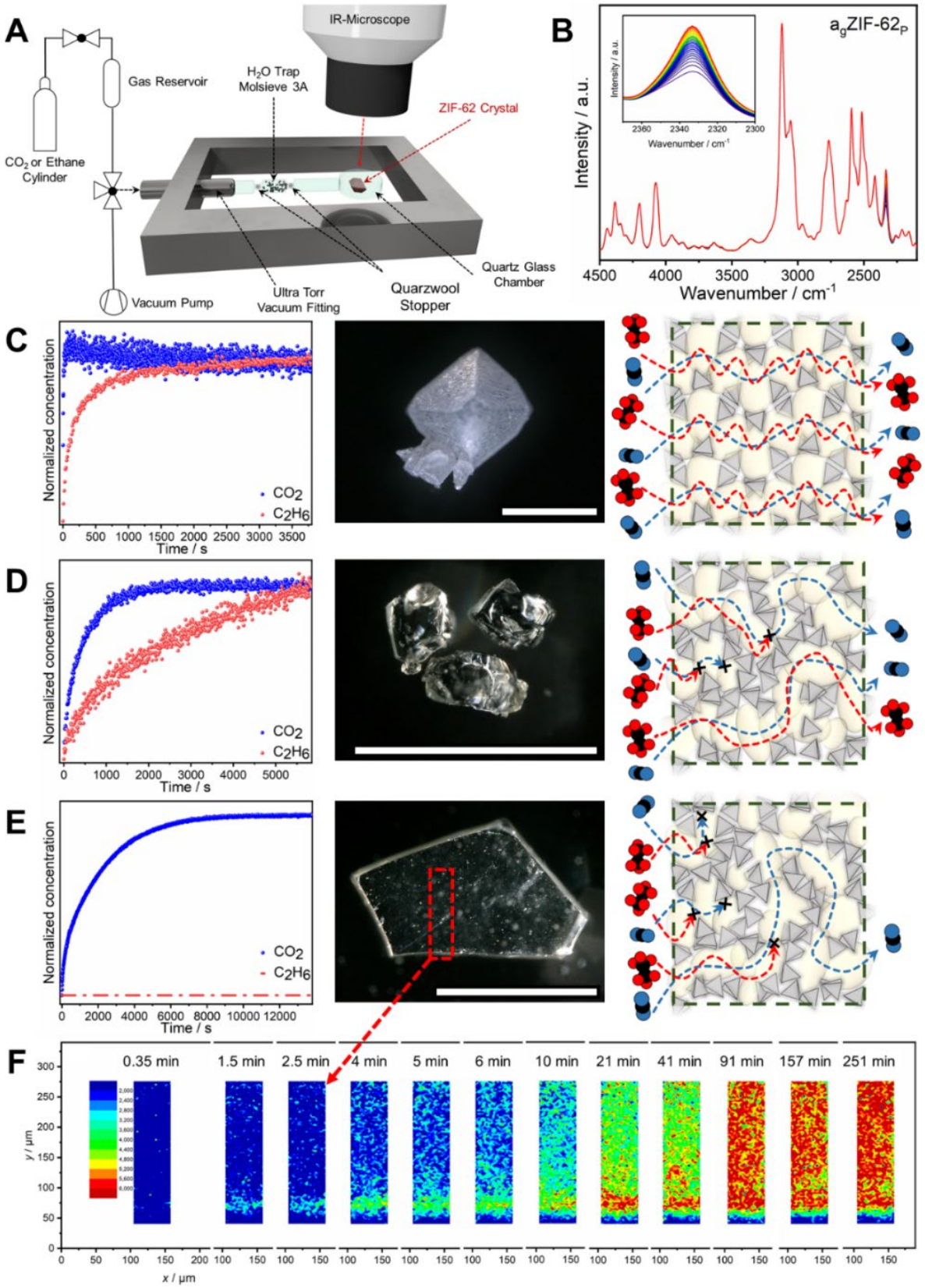

Fig. 2 (A) Schematic of the *in situ* IRM setup. **(B)** Typical IR absorbance spectra to determine the kinetic gas uptake, visualizing the increase of CO_2 peak over time (for $a_gZIF\text{-}62_P$). **(C-E)** Normalized kinetic gas uptake curves for 0-40 mbar CO_2 and 0-200 mbar ethane in **(C)** ZIF-62 single crystal, **(D)** not pressed $a_gZIF\text{-}62_{nP}$ and **(E)** pressed $a_gZIF\text{-}62_P$ with their corresponding microscopy images and schematics on the presumable changes of the porous structure and

gas pathways; all scalebars are 1 mm. **(F)** Guest concentration mapping upon CO_2 uptake over 250 min in a_gZIF-62_P on the edge of a glass shard.

The accessible porosity in the neat ZIF-62 crystal allows for very fast CO_2 uptake (kinetic diameter 3.3 Å), but moreover, allows ethane (4.16 Å) to enter the pores as well (**Fig. 2C**). In this case, a kinetic difference is visible, which we attribute to the different sizes of the molecules. Our data shows that the pore channels in crystalline ZIF-62 are much better accessible than previously thought (*20, 35, 36*). As for the amorphous samples, we still find a relatively fast uptake in a_gZIF-62_{nP} for CO_2, and slower uptake for ethane (**Fig. 2D**), which shows that size selectivity of the adsorption increases. This again is contradicting to prior findings, where the pore diameters and thereby apertures get significantly larger in a_gZIF-62 (*20, 34, 37*), whereas other data provide the hypothesis that short-range order deformation makes pores in a_gZIF-62 inaccessible (*18, 38*). The CO_2 diffusivity in this case is two orders of magnitude slower than this of the neat ZIF-62, which we attribute to a collapsing of the pore-channels. When melt-pressing a_gZIF-62_P, the CO_2 uptake becomes even slower than for a_gZIF-$62_{nP.}$ However, most importantly, no ethane uptake was detected for a_gZIF-62_P and a total exclusion was achieved. We show that compressing the liquid ZIF-62-glass results in smaller pore openings, which completely stops ethane entering (**Fig. 2E**). These findings show already a sharp molecular sieving cut-off between CO_2 and ethane, which offers tremendous potential for molecular sieving with amorphous MOFs.

Gas diffusion into a glass shard of a_gZIF-62_P (thickness = 200 µm) was investigated by guest concentration mapping through IR microimaging to monitor the evolution of CO_2 distribution inside the sample (**Fig. 2F**)**.** In the separate IR maps, the local CO_2 concentration is tracked by IR signals of guest molecules in the glass shard (blue color means relatively low CO_2 concentration and red color relatively high CO_2 concentration), at different times from 0.35 to 251 min. This data set confirms that the change of the pore channels in a_gZIF-62_P is macroscopically homogeneous throughout the whole sample. Moreover, this experiment reveals propagation of CO_2 molecules not only through the top and bottom surfaces, but also through the side of the glass shard (parallel to the long axis).

For both CO_2 and ethane, a clear trend is observed in diffusion: diffusion rate decreases with processing ZIF-62 > a_gZIF-62_{nP} > a_gZIF-62_P when the glass is derived directly from a crystal. These results prove that porosity structure of zeolitic imidazolate frameworks is strongly dependent on and is even controllable by the liquid handling process.

Tempering of ZIF glass

To determine the influence of temperature and time in liquid state on the pore structure, we heat treated previously obtained a_gZIF-62_{nP} and a_gZIF-62_P to tempered a_gZIF-$62_{nP\rightarrow T}$ and a_gZIF-$62_{P\rightarrow T}$ at 400 °C (above T_g). The samples were not grinded or milled for the best possible comparability. We find that tempering affects both types of samples in a similar way, resulting in a smoother shape because of the surface tension of the melt, but also some visible shrinking because of pore collapse. However, both a_gZIF-$62_{nP\rightarrow T}$ and a_gZIF-$62_{P\rightarrow T}$ remain

absolutely transparent after 2 hours of tempering with only a slight yellow shade appearing (**Fig. 3**, **A** to **C**).

CO_2 uptake studies were performed on the tempered samples and the diffusion was followed by IR microscopy. As expected, a shrinking of the samples means a stronger pore collapse and thus, slower CO_2 uptake in diffusion measurements (**Fig. 3**, **D** and **E**). Both for a_gZIF-$62_{nP\rightarrow T}$ and a_gZIF-$62_{P\rightarrow T}$, tempering leads to the partial collapse of the pores, making some channels and pores inaccessible for the gas molecules, meaning the molecules need to take a longer pathway. However, we still find CO_2 diffusing through both samples; moreover, a_gZIF-$62_{nP\rightarrow T}$ (**Fig. S22**) still adsorbs ethane, while the pore structure of a_gZIF-$62_{P\rightarrow T}$ remains completely inaccessible for ethane, as expected from a_gZIF-62_P.

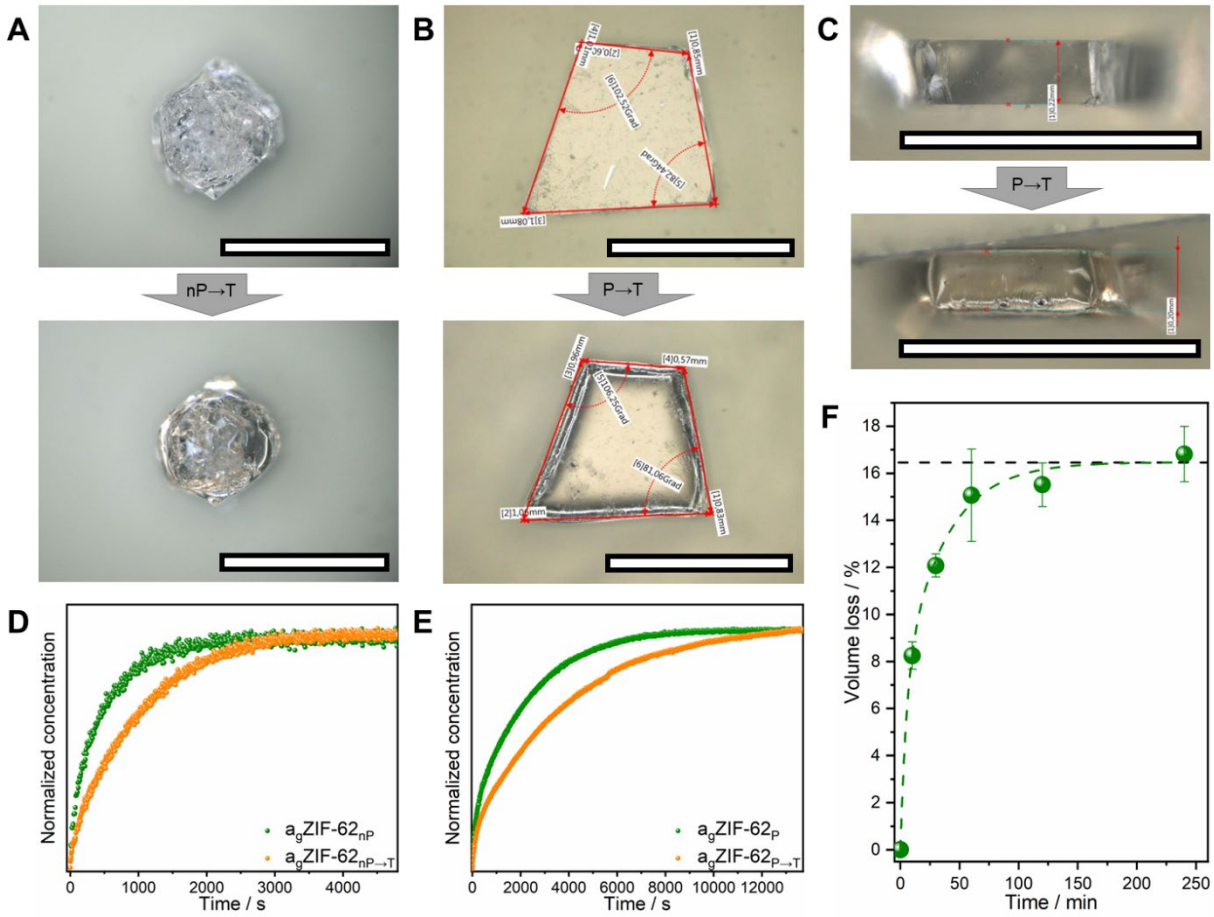

Fig. 3 (A) Micrographs of the same a_gZIF-62_{nP} sample before and after tempering a_gZIF-$62_{nP\rightarrow T}$; scalebars are 1 mm. **(B)** Top-view microscope images of a_gZIF-62_P sample before and after tempering a_gZIF-$62_{P\rightarrow T}$. **(C)** Micrographs of the side-views corresponding to **B**. All scalebars are 1 mm. **(D)** Kinetic CO_2 uptake from 0-40 mbar measured by the IRM for a_gZIF-$62_{nP\rightarrow T}$ and a_gZIF-62_{nP}. **(E)** The 0-40 mbar CO_2 uptake measured by the IRM for a_gZIF-$62_{P\rightarrow T}$ and a_gZIF-62_P. **(F)** Volume loss over tempering time for geometrically measured (*ex situ*) a_gZIF-$62_{P\rightarrow T}$ samples, with the size of a_gZIF-62_P taken for point (0,0).

As mentioned above, the tempering of a_gZIF-62_P to a_gZIF-$62_{P\rightarrow T}$ at 400 °C for 2h results in a rounding of edges and shrinking upon tempering in the top view (**Fig. 3B**) and when

looking from the side (**Fig. 3C**)**.** We took five shards of the same a_gZIF-62_P sample and observed the tempering process a_gZIF-$62_{P\rightarrow T}$ at 400 °C at different times for up to 4h (**SI Methods**). Tempering resulted in shrinking of the a_gZIF-$62_{P\rightarrow T}$ sample in all 3 dimensions (**Fig. S12** to **S16**, **Table S1**). These experiments show a rapid volume loss of about 16% with increasing tempering time that reaches a saturation threshold already after 2 hours. An exponential decay function was used to fit the decay of the volume (**Fig. 3F**). Further, the shrinking is optically visible on micrographs after 4 h, showing crumbled surfaces (**Fig. S16**, **Movie S5**). This data suggests that a controlled tempering program can be used to tailor molecular sieving properties of ZIF-62-derived glasses very precisely. Along with the fact that different pressures applied will obviously result in different gas transport abilities, ZIF-62 can be considered as an almost universal molecular sieve for permanent gases.

When tempering a_gZIF-62_{nP} in air atmosphere, all gas diffusion rates increase as this leads to a partial decomposition of the glasses, opening up channels and cavities for the diffusive gas transport (**Fig. S23** and **S24**).

Diffusivities in ZIF-62 and a_gZIF-62 materials

Diffusivities were calculated for all five samples, ZIF-62, a_gZIF-62_{nP}, a_gZIF-62_P, a_gZIF-$62_{nP\rightarrow T}$ (2h) and a_gZIF-$62_{P\rightarrow T}$ (2h) based on the kinetic CO_2 and ethane uptake (where applicable) (**Table 1**). Although ethane uptake was clearly observed in a_gZIF-62_{nP} and a_gZIF-$62_{nP\rightarrow T}$ (**Fig. S22**), determining its diffusivity was not flawlessly possible due to extremely slow uptake – it did not reach equilibrium within the given experiment duration of ca. 6 hours. Such slow uptake is possibly related to the capillary condensation in the small pores of the sample, where highly confined gas molecules become a liquid, which is a quite common effect in porous materials (*39*). As expected, crystalline ZIF-62 shows the highest diffusivity, which differs from all other samples by at least two orders of magnitude; the lowest belongs to a_gZIF-$62_{P\rightarrow T}$. Among a_gZIF-62_{nP}, a_gZIF-62_P and a_gZIF-$62_{nP\rightarrow T}$, CO_2 diffusivities do not differ drastically but noticeably and a more pronounced decrease is observed for a_gZIF-$62_{P\rightarrow T}$. This demonstrates again that the pore-channels in ZIF-glasses can be adjusted with a very high precision.

We used a He-pycnometer to determine the density of crystals and glasses including He-accessible porosity. Further, we measured the samples envelope density following the Archimedes principle using bulky toluene as solvent; the volume includes porosity of the matrix, as toluene cannot penetrate through the pore windows of ZIF-62 and ZIF-62-glasses.

Table 1 Measured physical properties of ZIF-62, a_gZIF-62$_{nP}$, a_gZIF-62$_P$, a_gZIF-62$_{nP\rightarrow T}$, a_gZIF-62$_{P\rightarrow T}$: Diffusion coefficients of CO_2 and ethane (*uptake measured, but diffusivity is impossible to calculate due to extremely slow uptake); skeletal and envelope densities.

Physical property	**ZIF-62**	**a_gZIF-62$_{nP}$**	**a_gZIF-62$_P$**	**a_gZIF-62$_{nP\rightarrow T}$**	**a_gZIF-62$_{P\rightarrow T}$**
Diffusivity CO_2 (m^2/s)	5.12×10^{-10}	3.53×10^{-12}	2.81×10^{-12}	2.09×10^{-12}	8.92×10^{-13}
Diffusivity ethane (m^2/s)	3.82×10^{-12}	n.a.*	n.a.	n.a.*	n.a.
Skeletal density (g/cm^3)	1.4728	1.4163	1.5250	1.4248	1.5316
	1.3903	← *Corrected by TG mass loss (5.6 wt%)*			
Envelope density (g/cm^3)	1.4178	1.3469	1.4458	1.3557	1.4556
	1.3384	← *Corrected by TG mass loss (5.6 wt%)*			

Destabilization of ZIF-62 to ZIF-62 glass and stability of the melt

As expected, the skeletal He-density in porous materials is always higher than the envelope density. In case of ZIF-62 and the ZIF-62-glasses, the two types of density are also changing proportionally (**Fig. 4A**). All density values are given in **Table 1**. Envelope density of a_gZIF-62$_{nP}$ of 1.3469 g/cm^3, is in good accordance with the recently discovered data, which was determined as 1.35 g/cm^3 from CO_2 sorption experiments (*37*). Envelope and skeletal densities of the crystalline ZIF-62 were found to be 1.4178 g/cm^3 and 1.4728 g/cm^3 respectively, being noticeably higher than the calculated crystallographic density from the same work (1.29 g/cm^3) (*37*). We suppose that such a contradiction might be caused by the difference between simulated crystalline matrix and real object. Based on the TGA data (**Fig. 4B**) which have been collected together with DSC (**Fig. 1F**), a 5.6% mass loss occurs at the thermal amorphization point of ZIF-62 at 330 °C. We think that the amorphization prior to glass transition which has been described previously (*33*), is based on desolvation of structurally important guests. Similar to ZIF-90 (*40*), the ZIF-62 structure seems to be supported by guest molecules with limited periodicity. Therefore, the mass loss at the initial amorphization point needs to be considered as crucial for the destabilization of ZIF-62 and the values must be corrected by the stabilizing guest molecules to derive an estimate, guest-free crystal density (**Fig. 4A**). We investigated the mass loss during melting by DSC coupled mass spectrometry (MS), which shows that it is only associated with the desolvation of guest molecules. Thereby, low amounts of DMF and its fragments leave the crystal, but also – unexpectedly, as ZIF-62 should be hydrophobic – water is confirmed by the mass spectrometry data (**Fig. 4C**). Even though the DSC-MS is operated under N_2 atmosphere, a low level of oxygen and water cannot be excluded. A burst release of water molecules and CO_2 from the framework is found from 320-330 °C, meaning that these molecules are strongly adsorbed in the framework. Interestingly, the oxygen level shows a sudden loss later, at 350°C after the amorphization temperature, which might be attributed to capping open metal sides in the

amorphized framework, leaving Zn-O bridges undetectable with PXRD, again because of limited periodicity. After that point, the melting at 450°C happens without any changes. Additionally, we measured DSC-MS for the tempering over 240 min at 400°C for a_gZIF-62_{nP} (**Fig. 4D**) and a_gZIF-62_P (**Fig. S25**). Neither desolvation nor decomposition with mass-loss occurs during tempering, proving that the glass is highly stable during its processing under inert atmosphere, making it suitable for all kinds of applications. Overall, we detect no linkers disappearing from the lattice, nor any decomposition of the remaining structure under inert conditions below 500°C. A desolvation/fragmentation of crucial structurally stabilizing moieties from the pores leads first to an amorphization (*33*) and then later to melting of the framework.

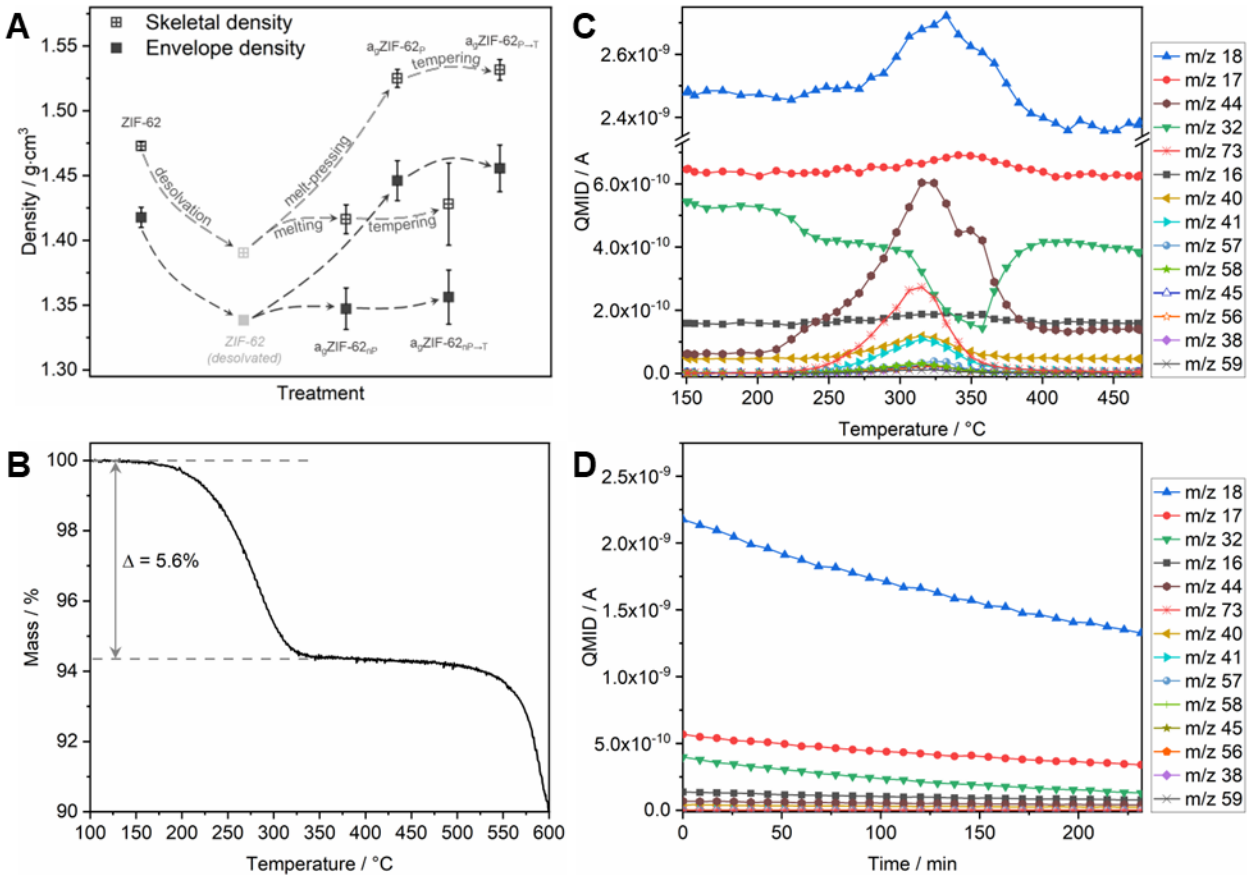

Fig. 4 (A) Skeletal and envelope densities of ZIF-62 and ZIF-62-derived samples following the treatment processes schematically on the x-axis. **(B)** TGA/DSC mass loss curve for ZIF-62. **(C)** Mass spectrometry data for ZIF-62 upon heating above the melting point. **(D)** Mass spectrometry data for a_gZIF-62_{nP} tempering.

Discussion

We demonstrated the scalability of crystalline ZIF-62 and the processing towards ZIF-glass sheet and films with homogeneous pore channels that are tailorable through glass processing. Using millimeter-sized single crystals in this study, we were able to determine diffusion coefficients of CO_2 and ethane and provide evidence for size exclusion in ZIF-62 glasses, which demonstrates the tremendous potential for molecular sieving of the tiniest

molecules. The ZIF-glass would have strong benefits over a polycrystalline ZIF-62 film: no more grain boundaries that lead to defect diffusion, and better molecular sieving capabilities even though it is an amorphous material. Through the demonstrated scalability of bulk ZIF-62, membranes can be easily made as liquid processing paves the way for large scale productions. By changing the processing parameters of the ZIF-62-glass, the collapse of the pores is highly controllable and allows to reach an Å-scale resolution for molecular sieving. Depending on the processing parameters applied to the liquified ZIF-62, be it temperature, pressure (or both), the nanopore channels of the resulting glasses can be controlled to totally exclude sterically demanding gas, such as ethane. This may become extremely interesting when looking at challenging separations, such as H_2/He from natural gas. Obviously interesting are all kinds of CO_2 separation, such as H_2/CO_2, N_2/CO_2 or even direct CO_2 capture from air. We demonstrate that these glasses can be processed to be destruction-free and kept under inert conditions at the melting point more than long enough to get monolithic pieces. With such isotropic, microporous glasses we might be able to a develop liquid processable, free-standing MOF membranes made from 100 % bulk MOF and tackle modern, important separation challenges, such as direct air capture of CO_2 or He in a continuous and energy-efficient membrane separation process.

References

1. X. Sun *et al.,* Metal-Organic Framework Mediated Cobalt/Nitrogen-Doped Carbon Hybrids as Efficient and Chemoselective Catalysts for the Hydrogenation of Nitroarenes. *ChemCatChem*. **9**, 1854–1862 (2017), doi:10.1002/cctc.201700095.
2. A. Knebel *et al.,* Solution processable metal-organic frameworks for mixed matrix membranes using porous liquids. *Nat. Mater.* **19**, 1346–1353 (2020), doi:10.1038/s41563-020-0764-y.
3. D. P. Erdosy *et al.,* Microporous water with high gas solubilities. *Nature*. **608**, 712–718 (2022), doi:10.1038/s41586-022-05029-w.
4. T. D. Bennett *et al.,* Melt-Quenched Glasses of Metal-Organic Frameworks. *J. Am. Chem. Soc.* **138**, 3484–3492 (2016), doi:10.1021/jacs.5b13220.
5. T. D. Bennett *et al.,* Hybrid glasses from strong and fragile metal-organic framework liquids. *Nat. Commun.* **6**, 8079 (2015), doi:10.1038/ncomms9079.
6. L. Wondraczek, J. C. Mauro, Advancing glasses through fundamental research. *J. Eur. Ceram. Soc.* **29**, 1227–1234 (2009), doi:10.1016/j.jeurceramsoc.2008.08.006.
7. S. Li *et al.,* Mechanical Properties and Processing Techniques of Bulk Metal-Organic Framework Glasses. *J. Am. Chem. Soc.* **141**, 1027–1034 (2019), doi:10.1021/jacs.8b11357.
8. T. To *et al.,* Fracture toughness of a metal-organic framework glass. *Nat. Commun.* **11**, 2593 (2020), doi:10.1038/s41467-020-16382-7.
9. R. Freund *et al.,* 25 Years of Reticular Chemistry. *Angew. Chem. Int. Ed.* **60**, 23946–23974 (2021), doi:10.1002/anie.202101644.
10. A. Knebel, J. Caro, Metal-organic frameworks and covalent organic frameworks as disruptive membrane materials for energy-efficient gas separation. *Nat. Nanotechnol.* **17**, 911–923 (2022), doi:10.1038/s41565-022-01168-3.
11. S. Zhou *et al.,* Asymmetric pore windows in MOF membranes for natural gas valorization. *Nature*. **606**, 706–712 (2022), doi:10.1038/s41586-022-04763-5.
12. A. Knebel *et al.,* Defibrillation of soft porous metal-organic frameworks with electric fields. *Science*. **358**, 347–351 (2017), doi:10.1126/science.aal2456.
13. A. W. Thornton *et al.,* Porosity in metal-organic framework glasses. *Chem. Commun.* **52**, 3750–3753 (2016), doi:10.1039/c5cc10072k.
14. C. Zhou *et al.,* Metal-organic framework glasses with permanent accessible porosity. *Nat. Commun.* **9**, 5042 (2018), doi:10.1038/s41467-018-07532-z.
15. L. Longley *et al.,* Flux melting of metal-organic frameworks. *Chem. Sci.* **10**, 3592–3601 (2019), doi:10.1039/c8sc04044c.
16. V. Nozari *et al.,* Low-Temperature Melting and Glass Formation of the Zeolitic Imidazolate Frameworks ZIF-62 and ZIF-76 through Ionic Liquid Incorporation. *Adv. Mater. Technol.*, 2200343 (2022), doi:10.1002/admt.202200343.
17. V. Nozari *et al.,* Ionic liquid facilitated melting of the metal-organic framework ZIF-8. *Nat. Commun.* **12**, 5703 (2021), doi:10.1038/s41467-021-25970-0.
18. R. S. K. Madsen *et al.,* Ultrahigh-field 67Zn NMR reveals short-range disorder in zeolitic imidazolate framework glasses. *Science*. **367**, 1473–1476 (2020), doi:10.1126/science.aaz0251.
19. A. Qiao *et al.,* A metal-organic framework with ultrahigh glass-forming ability. *Sci. Adv.* **4**, eaao6827 (2018), doi:10.1126/sciadv.aao6827.
20. Y. Wang *et al.,* A MOF Glass Membrane for Gas Separation. *Angew. Chem. Int. Ed.* **59**, 4365–4369 (2020), doi:10.1002/anie.201915807.
21. H. Xia *et al.,* A long-lasting TIF-4 MOF glass membrane for selective CO2 separation. *J. Mem. Sci.* **655**, 120611 (2022), doi:10.1016/j.memsci.2022.120611.
22. V. Nozari, C. Calahoo, L. Longley, T. D. Bennett, L. Wondraczek, Structural integrity, meltability, and variability of thermal properties in the mixed-linker zeolitic imidazolate framework ZIF-62. *J. Chem. Phys.* **153**, 204501 (2020), doi:10.1063/5.0031941.
23. C. Healy *et al.,* The thermal stability of metal-organic frameworks. *Coord. Chem. Rev.* **419**, 213388 (2020), doi:10.1016/j.ccr.2020.213388.
24. R. S. K. Madsen *et al.,* Mixed metal node effect in zeolitic imidazolate frameworks. *RSC Adv,*. **12**, 10815–10824 (2022), doi:10.1039/d2ra00744d.

25. M. Stepniewska, M. B. Østergaard, C. Zhou, Y. Yue, Towards large-size bulk ZIF-62 glasses via optimizing the melting conditions. *J. Non Cryst. Solids*. **530**, 119806 (2020), doi:10.1016/j.jnoncrysol.2019.119806.
26. L. Frentzel-Beyme *et al.,* Porous purple glass – a cobalt imidazolate glass with accessible porosity from a meltable cobalt imidazolate framework. *J. Mater. Chem. A*. **7**, 985–990 (2019), doi:10.1039/C8TA08016J.
27. J.-B. Lin *et al.,* A scalable metal-organic framework as a durable physisorbent for carbon dioxide capture. *Science*. **374**, 1464–1469 (2021), doi:10.1126/science.abi7281.
28. S. Berens *et al.,* Ethane diffusion in mixed linker zeolitic imidazolate framework-7-8 by pulsed field gradient NMR in combination with single crystal IR microscopy. *PCCP*. **20**, 23967–23975 (2018), doi:10.1039/c8cp04889d.
29. C. Chmelik *et al.,* Nanoporous glass as a model system for a consistency check of the different techniques of diffusion measurement. *Chem. Phys. Chem.* **12**, 1130–1134 (2011), doi:10.1002/cphc.201100072.
30. T. Titze *et al.,* Transport in Nanoporous Materials Including MOFs: The Applicability of Fick's Laws. *Angew. Chem. Int. Ed.* **54**, 14580–14583 (2015), doi:10.1002/anie.201506954.
31. B. Birner, J. Severinghaus, B. Paplawsky, R. F. Keeling, Increasing atmospheric helium due to fossil fuel exploitation. *Nat. Geosci.* **15**, 346–348 (2022), doi:10.1038/s41561-022-00932-3.
32. M. Gustafsson, X. Zou, Crystal formation and size control of zeolitic imidazolate frameworks with mixed imidazolate linkers. *J. Por. Mater.* **20**, 55–63 (2013), doi:10.1007/s10934-012-9574-1.
33. R. N. Widmer *et al.,* Pressure promoted low-temperature melting of metal-organic frameworks. *Nat. Mater.* **18**, 370–376 (2019), doi:10.1038/s41563-019-0317-4.
34. L. Frentzel-Beyme, M. Kloß, P. Kolodzeiski, R. Pallach, S. Henke, Meltable Mixed-Linker Zeolitic Imidazolate Frameworks and Their Microporous Glasses: From Melting Point Engineering to Selective Hydrocarbon Sorption. *J. Am. Chem. Soc.* **141**, 12362–12371 (2019), doi:10.1021/jacs.9b05558.
35. J. Gandara-Loe, R. Bueno-Perez, A. Missyul, D. Fairen-Jimenez, J. Silvestre-Albero, Molecular Sieving Properties of Nanoporous Mixed-Linker ZIF-62: Associated Structural Changes upon Gas Adsorption Application. *ACS Appl. Nano Mater.* **4**, 3519–3528 (2021), doi:10.1021/acsanm.1c00010.
36. R. Banerjee *et al.,* High-throughput synthesis of zeolitic imidazolate frameworks and application to CO2 capture. *Science*. **319**, 939–943 (2008), doi:10.1126/science.1152516.
37. L. Frentzel-Beyme, P. Kolodzeiski, J.-B. Weiß, A. Schneemann, S. Henke, Quantification of gas-accessible microporosity in metal-organic framework glasses. *Nat. Commun.* **13**, 7750 (2022), doi:10.1038/s41467-022-35372-5.
38. Z. Shi, A. Arramel, T. D. Bennett, Y. Yue, N. Li, The deformation of short-range order leading to rearrangement of topological network structure in zeolitic imidazolate framework glasses. *iScience*. **25**, 104351 (2022), doi:10.1016/j.isci.2022.104351.
39. Q. Yang *et al.,* Capillary condensation under atomic-scale confinement. *Nature*. **588**, 250–253 (2020), doi:10.1038/s41586-020-2978-1.
40. W. Morris, C. J. Doonan, H. Furukawa, R. Banerjee, O. M. Yaghi, Crystals as molecules: postsynthesis covalent functionalization of zeolitic imidazolate frameworks. *J. Am. Chem. Soc.* **130**, 12626–12627 (2008), doi:10.1021/ja805222x.

Acknowledgement

The authors thank Thomas D. Bennett for stimulating discussions. O.S., S.S., L.W. and A.K. are grateful for support through the Carl-Zeiss Foundation within the "Breakthroughs" program. S.H., C.C. and J.K. acknowledge support by the Deutsche Forschungsgemeinschaft (grant HA 1893/25-1). We thank Nadja Greiner-Mai for her technical support. We thank the NMR Platform of the University of Jena.